Formation and cation distribution in supported manganese ferrite nanoparticles: an X-ray absorption study†

Daniela Carta, Maria Francesca Casula, Gavin Mountjoy‡ and Anna Corrias*

Received 9th January 2008, Accepted 11th March 2008
First published as an Advance Article on the web 10th April 2008
DOI: 10.1039/b800359a

Extended X-ray absorption fine structure (EXAFS) and X-ray absorption near-edge structure (XANES) techniques at both Fe and Mn K-edges were used to investigate the formation of $MnFe_2O_4$ nanoparticles embedded in a silica aerogel matrix as a function of calcination temperature (at 450, 750 and 900 °C). Up to 450 °C, two separated highly-disordered phases of iron and manganese are present. With increasing the temperature (to 750 and 900 °C), the structure of aerogel nanoparticles becomes progressively similar to that of the spinel structure $MnFe_2O_4$ (jacobsite). Quantitative determination of cations distribution in the spinel structure shows that aerogels calcined at 750 and 900 °C have a degree of inversion $i = 0.20$. A pure jacobsite sample synthesised by co-precipitation and used as a reference compound shows a much higher degree of inversion ($i = 0.70$). The different distribution of iron and manganese cations in the octahedral and tetrahedral sites in pure jacobsite and in the aerogels can be ascribed to partial oxidation of Mn^{2+} to Mn^{3+} in pure jacobsite, confirmed by XANES analysis, probably due to the synthesis conditions.

Introduction

Transition-metal ferrites, MFe_2O_4 (where M = Co, Ni, Mn, Mg, Zn *etc.*), are a class of oxides which have the spinel structure.† In recent years, they have been an important subject of research for their remarkable magnetic, optical and electrical properties. In particular, nanocrystalline transition-metal ferrites exhibit unique properties such as size-dependent superparamagnetic behaviour.[1] Moreover, the increased miniaturisation and data-storage density of novel devices requires the use of nanosized magnetic particles. Transition-metal ferrite nanoparticles find applications in magnetic-storage devices,[2] site-specific drug delivery,[3] magnetic-resonance imaging[4] and photomagnetic materials.[5]

Manganese ferrite nanoparticles ($MnFe_2O_4$) have received increasing attention for their remarkable magnetic properties, $MnFe_2O_4$ being a soft-magnetic material (low coercivity, moderate saturation magnetisation), combined with a good chemical stability and mechanical hardness.[6] Nanocrystalline manganese ferrite can be prepared by ball-milling of Mn_2O_3 and Fe_2O_3,[7] the hydrothermal route[8] and coprecipitation.[9] It has been shown that nanocrystalline $MnFe_2O_4$ prepared by ball-milling or wet-precipitation methods has different properties than the bulk $MnFe_2O_4$ synthesised by the traditional solid-state reaction at high temperature.[10]

Dipartimento di Scienze Chimiche and INSTM, Università di Cagliari, S.P. Monserrato-Sestu Km 0.700, I-09042 Monserrato, Cagliari, Italy. E-mail: corrias@unica.it

† Electronic supplementary information (ESI) available: XANES spectra of standards and a drawing of a spinel structure. See DOI: 10.1039/b800359a

‡ Permanent address: School of Physical Sciences, Ingram Building, University of Kent, Canterbury, UK CT2 7NH

Non-supported manganese ferrite nanoparticles have the tendency to aggregate and grow, and this can result in a negative effect on the magnetic properties. In order to avoid aggregation, the nanoparticles can be homogeneously dispersed in a matrix, giving rise to magnetic nanocomposite materials. Magnetic nanocomposites have peculiar and tuneable properties, mainly depending on particle size and distribution of the nanocrystals, morphology and porosity of the matrix and interaction of the nanocrystals and the matrix.

Composites of ferrite nanoparticles dispersed in a silica matrix have been successfully obtained by the sol–gel route.[11–13] Good control of composition, purity, homogeneity, particle sizes and distribution can be obtained. Most of the works published so far follow the traditional sol–gel route, where the drying of the gels is performed by thermal treatment (xerogels); this causes cracking of the gels and collapse of the porous structure. However, the preservation of the porous structure is quite important, especially for avoiding interactions between the magnetic nanoparticles and for applications where the surface area plays a very important role.

The samples studied in this work are nanocomposites containing $MnFe_2O_4$ dispersed in a very highly porous silica host obtained by the sol–gel route through supercritical drying of the gel. The use of this special drying technique avoids the capillary forces at the liquid/vapour interface responsible for the formation of cracks and the collapse of the porous structure. Therefore, the products after drying (aerogels) present low densities, high porosities and high surface areas. An interesting application of nanoparticles of manganese ferrite in an aerogel network is the separation of gas-phase analytes based on magnetic interactions.[14] In this work, aerogels containing 10 wt% $MnFe_2O_4/(MnFe_2O_4 + SiO_2)$ calcined in argon at increasing temperatures (450, 750 and 900 °C) were

studied. Evolution of the aerogel systems with calcination temperature has been studied using extended X-ray absorption fine structure (EXAFS) and X-ray absorption near-edge structure (XANES) spectroscopies.

EXAFS and XANES have been shown to be powerful tools for the structural study of metal oxide nanoparticles and nanocomposites prepared by the sol–gel process.[15–21] These techniques are element-specific and sensitive to the local structure,[22] making them ideal for studying multicomponent dilute and disordered materials. EXAFS gives information about bond distances and coordination numbers of shells surrounding the absorbing atom; XANES gives information on symmetry and the oxidation state of the absorbing atom. Moreover, EXAFS has been recently found to be a useful tool to determine the cation distribution in ferrite spinels.[23–25] In the structure of ferrites, cations (bivalent and trivalent) reside on the tetrahedral and octahedral sites available in the close packing of oxygen anions. The cation distribution is defined by the inversion parameter *i* which indicates the fraction of trivalent cations in tetrahedral sites. The cation distribution between octahedral and tetrahedral sites can vary and crucially influences the catalytic, magnetic and electronic properties. Information on cation distribution can be obtained using a variety of probes such as X-ray (XRD) and neutron diffraction[26] and Mössbauer spectroscopy.[27] However, the usefulness of XRD is limited by the similar scattering factors of Mn and Fe and by the nanodimension of the particles that broadens the peaks. Mössbauer spectroscopy is effective in determining the environment of Fe ions but does not provide information on the Mn cations and is not very effective for dilute samples.[28] Therefore, we decided to make use of EXAFS which seems the most promising technique for studying the cation site distribution of manganese ferrite nanoparticles dispersed in an amorphous matrix, since it allows one to study the environment around the Fe and Mn ions separately and independently.

2. Experimental

2.1 Sample preparation

The samples were prepared by a sol–gel process recently developed for $CoFe_2O_4$–SiO_2 highly porous aerogel nanocomposites.[29] The preparation involves the use of tetraethoxysilane [($Si(OC_2H_5)_4$, Aldrich 98%, TEOS] as a precursor for silica, iron(III) and manganese(II) nitrates ($Fe(NO_3)_3{\cdot}9H_2O$, Aldrich, 98% and $Mn(NO_3)_2{\cdot}6H_2O$, Aldrich, 98%) as precursors for the manganese ferrite phase and absolute ethanol (EtOH, Fluka) as mutual solvent. The precursors were added in such a way to obtain nanocomposites containing a nominal ratio of 10 wt% $MnFe_2O_4/(MnFe_2O_4 + SiO_2)$. The ethanolic solution of the metal salts was added into the pre-hydrolysed TEOS under acidic catalysis. Urea (NH_2CONH_2, Aldrich, >99.0%) was then added under reflux for 2 h at 85 °C as a basic gelation agent. The sols were left in a closed container at 40 °C; gelation occurred in less than 2 days. The alcogels were submitted to high-temperature supercritical drying in an autoclave (Parr, 300 cm^3). The autoclave was filled with an appropriate amount of ethanol and flushed with N_2 before being heated in such a way to take the solvent to the supercritical state (*i.e.* 330 °C, 70 atm). The autoclave was then vented and highly porous aerogel samples were obtained. The samples were calcined in argon at 450 °C for 1 h, 750 °C (for 2 and 20 h) and 900 °C for 1 h. The aerogels will be hereafter called A_YYY, where YYY refers to the calcination temperature. Two aerogels containing only iron and only manganese (10 wt%) in a silica matrix were also prepared with the same procedure and calcined at 450 °C. These will be hereafter called AFe_450 and AMn_450 respectively.

A pure jacobsite sample to be used as a reference was prepared according to the method described in ref. 30. Briefly, an aqueous solution of $FeCl_3{\cdot}H_2O$ and $MnCl_2{\cdot}H_2O$ was poured into a NaOH solution, under magnetic stirring. The precipitated obtained was digested in a water bath at 90 °C for about 90 min and then washed, filtered and dried at 50 °C.

2.2 X-Ray diffraction data collection (XRD)

XRD spectra were recorded on a X3000 Seifert diffractometer equipped with a graphite monochromator on the diffracted beam. The scans were collected within the range of 10–80 degrees (2ϑ) using Cu Kα radiation.

2.3 X-Ray absorption data collection (XANES and EXAFS)

The X-ray absorption spectroscopy experiments were carried out on station 7.1 of the SRS, Daresbury Laboratory, UK. Data were collected at room temperature using a Si(111) monochromator at the Fe (7112 eV) and Mn (6539 eV) K-edges.

Data were collected on aerogel samples, calcined at 450, 750 (2 and 20 h) and 900 °C. Data were also collected on a pure manganese ferrite as a reference compound.

Samples with a suitable and highly uniform optical thickness were prepared from powders. In the case of the reference samples the powders were dispersed in an inert solvent and then filtered onto polythene supports. The aerogel samples were pressed into a cardboard frame with mylar windows without the need of using any diluent, the aerogels being very easy to compress due to their very low apparent density.

2.4 XANES data analysis

The XANES spectra were processed in the usual way to obtain normalised absorbance.[31] XANES at the K-edge involves the excitation of a 1s photoelectron into low-lying empty states at the central atom with p-type symmetry. The K-edge XANES spectra in transition metals has a gradually sloping main absorption edge, with a pronounced step on the low-energy side, a rounded main-absorption-edge peak, and approximately constant intensity following the edge. In contrast, transition-metal oxides have a sharply rising main absorption edge, with main-absorption-edge peak(s) of high intensity, and a notable drop in intensity after the main-absorption-edge peak. In addition, oxides may show a small pre-edge peak if the excited atom site has a lack of centrosymmetry. In both metals and oxides, oscillations in intensity occurring up to approx. 30 eV beyond the absorption edge are due to strong multiple-scattering or shape resonance around the excited atom site. The XANES spectra have been analysed using the

"fingerprint" method, by comparing spectra from samples with those from reference compounds.

2.5 EXAFS data analysis

The program Viper was used to sum the data, identify the beginning of the absorption edge (E_0), fit pre- and post-edge backgrounds, and hence to obtain the normalised absorbance χ as a function of the modulus of the photoelectron wavevector k.[32] The modular package DL_EXCURV,[33] based on the EXCURV98 code, was used in the final stage of data processing to model the experimental $\chi(k)$ in order to extract structural information. This code uses fast curved-wave theory[34] and calculates *ab initio* the effective curved-wave backscattering amplitude of the scatterer, the phase shift due to the absorbing atom potential, the phase shift due to the scatterer, and the inelastic mean free path of the photoelectron.[35,36] In DL_EXCURV the k-independent parameter AFAC (amplitude reduction due to many electron processes) was determined to be 0.9 from fitting to the reference samples. The parameter EF, which is a correction to E_0, was free to vary in all fitting. The structural parameters were obtained by non-linear least-squares fitting in k-space with a k^3 weighting of the total experimental EXAFS spectra to emphasise the high-energy part of the spectrum. The fitting was carried out using the k range 2.5–12 Å^{-1}. The errors in the fit parameters, R_i, N_i and $2\sigma_i^2$, were obtained from the 95% confidence level[37] as calculated in EXCURV98. The number of fitted parameters was always less than the number of statistically independent data points, as estimated in the standard way.[37]

The quality of the fit was judged from the normalised sum of residuals

$$R\text{-factor} = \Sigma_n k_n^3 |\chi_{\text{expt}}(k_n) - \chi_{\text{fit}}(k_n)| / \Sigma_n k_n{}^3 |\chi_{\text{expt}}(k_n)| \times 100 \quad (1)$$

R-factors were calculated both on the experimental $k^3\chi(k)$ and on the data obtained by inverse-transforming the Fourier transforms in the R space corresponding to the shells which were fitted. The second value, named as $*R$, is more meaningful in stating the goodness of the fit since the back-transforms do not contain low R contributions due to imperfect background removal and high R contributions which were not introduced in the fitting. Reasonable EXAFS fits of single shells typically have R-factor values of around 20%; however, when the fit is performed on the total EXAFS spectra, higher values of R-factor can still correspond to good fits especially if the fit is not extended to peaks at high R.

3. Results

3.1 XRD

XRD patterns of aerogels after extraction, calcined at 450, 750 (2 and 20 h) and 900 °C along with the pure jacobsite are presented in Fig. 1. The pattern of aerogels after extraction and calcined at 450 °C just show the amorphous halo due to the silica matrix. In the sample after calcination at 750 °C for 2 h peaks corresponding to the jacobsite phase[38] appear superimposed on the amorphous silica halo. The peaks become more intense with the increase of calcination time and temperature. The peaks of the pure jacobsite sample

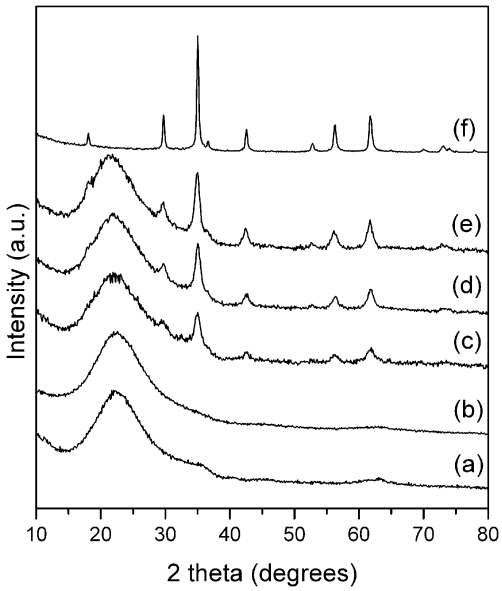

Fig. 1 XRD patterns of: A_ae (a), A_450 (b), A_750_2h (c), A_750_20h (d), A_900 (e), jacobsite (f).

are quite sharp indicating a larger particle size compared to the aerogels.

3.2 XANES

The XANES spectra for the pure jacobsite phase, for the A samples and for AFe and AMn are shown in Fig. 2A and B, at the Fe and Mn K-edges respectively. Information on the oxidation state of iron and manganese in the spinel structure has been obtained by comparing the absorption edge position with those of standard iron and manganese oxides of known oxidation states (reported as ESI†).

At the Fe edge, a comparison of the edge position of the pure jacobsite sample with those of different Fe oxides shows that the jacobsite edge position corresponds to that of γ-Fe_2O_3. Therefore, the oxidation state of iron in the pure jacobsite phase is +3, as expected. At the Mn edge, a comparison of the edge position of the same sample with those of different Mn oxides shows that the jacobsite edge position is slightly higher than for MnO and lower than for Mn_3O_4. This indicates that the pure jacobsite sample contains some Mn^{+3} in addition to Mn^{+2}.

At the Fe edge, the position of the absorption edges for all the aerogels correspond to that of pure jacobsite, typical of Fe^{+3}. The XANES of AFe_450, A_ae, A_450 are similar to each other and to ferrihydrite.[39] There is a clear progression from the A_450 towards A_900. The latter looks very similar to the pure jacobsite sample but the pre-edge peak is less pronounced, indicating some structural differences (see inset of Fig. 2A). In particular, it seems to indicate that the pure jacobsite sample has an higher percentage of iron in non-symmetrical sites (tetrahedral). At the Mn edge, there is a difference in the edge position of all the aerogels and pure jacobsite. The XANES profile of pure jacobsite is shifted to higher energies compared to all the aerogels, indicating an higher oxidation state of manganese. In particular, the absorption-edge positions of all aerogels are typical of Mn^{+2}.

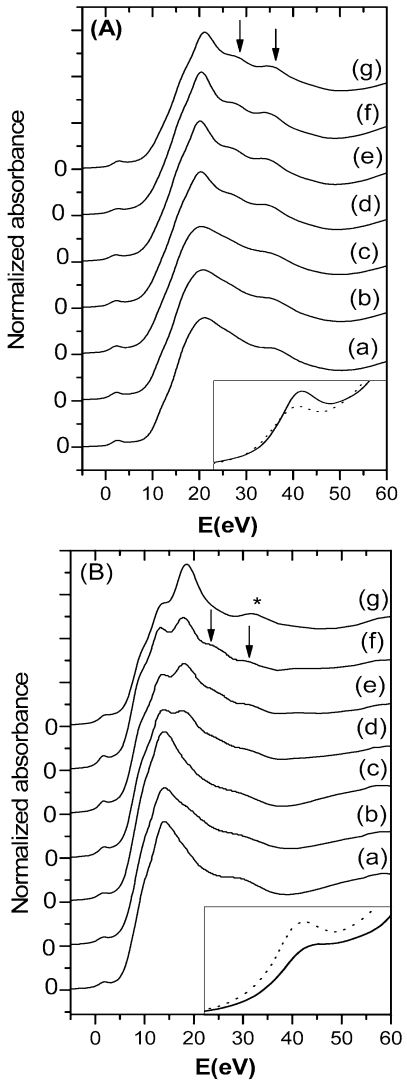

Fig. 2 XANES spectra at the Fe K-edge (A) and Mn K-edge (B) from experiment (—) and fit results (···). The value 0 eV corresponds to the energy of the first inflection point of the K-edge of Fe and Mn reference foils. (A): AFe_450 (a), A_ae (b), A_450 (c), A_750_2h (d), A_750_20h (e), A_900 (f), jacobsite (g). Inset: A_900 (f) (dotted line), jacobsite (g) (straight line). (B): AMn_450 (a), A_ae (b), A_450 (c), A_750_2h (d), A_750_20h (e), A_900 (f), jacobsite (g). Inset: A_900 (f) (dotted line), jacobsite (g) (straight line).

XANES profiles of AMn_450, A_ae, A_450 are similar to each other. As the temperature increases, A_750_2h, A_750_20h and A_900 become more similar to pure jacobsite. The Mn edge of A_900 looks similar to pure jacobsite, nevertheless there are noticeable differences. One of the differences is that the pre-edge peak is sharper in A_900 than in pure jacobsite (see inset in Fig. 2B). Another difference is that after the main-absorption-edge peak, the spectrum for pure jacobsite has only a single large peak located at 33 eV (see asterisk in Fig. 2B), whereas the spectrum for A_900 has two small peaks located at 23 and 32 eV (see arrows in Fig. 2B). The latter are similar to the two small peaks located at 28 and 37 eV in the Fe-edge spectrum of pure jacobsite (see arrows in Fig. 2A).

3.3 EXAFS

In Fig. 3A, the EXAFS spectra at the Fe K-edge for the AFe_450, A_ae, A_450, A_750_2h, A_750_20h and A_900 samples are shown along with that of the pure jacobsite reference compound.

The oscillations of AFe_450, A_ae and A_450 are quite weak and do not appear up to high k as observed for A_750_20h, A_900 and pure jacobsite. Moreover, both the frequencies and amplitudes of the oscillations in AFe_450 seem very similar to those of A_ae, which also look very similar to those of A_450. These oscillation frequencies and amplitudes look very similar to those of ferrihydrite (a poorly crystallised phase of iron(III) oxyhydroxide), the EXAFS spectrum of which has been reported in ref. 39. This is an indication that AFe_450, A_ae and A_450 are very poorly crystalline systems. This result is in agreement with the XRD

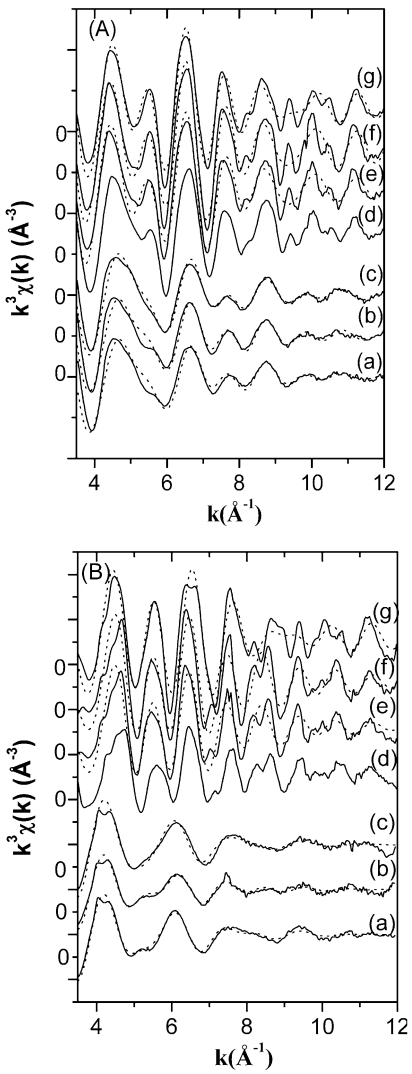

Fig. 3 $k^3\chi(k)$ spectra at the Fe K-edge (A) and Mn K-edge (B) from experiment (—) and fit results (···). (A): AFe_450 (a), A_ae (b), A_450 (c), A_750_2h (d), A_750_20h (e) A_900 (f), jacobsite (g). (B): AMn_450 (a), A_ae (b), A_450 (c), A_750_2h (d), A_750_20h (e) A_900 (f), jacobsite (g).

analysis. The oscillations of A_750_20h and A_900 arrive up to high k and are very similar to those of the pure jacobsite.

In Fig. 3B, the EXAFS spectra at the Mn K-edge for the AMn_450, A_ae, A_450, A_750_20h, A_900 samples are shown along with the reference compound jacobsite. The oscillations of AMn_450, A_ae and A_450 are similar to each other. They are weak and do not appear up to high k, indicating quite disordered structures. As the calcination temperature increases (A_750 and A_900), the oscillations become more similar to those of pure jacobsite.

Analysis of the Fourier transforms (FTs) at the Fe and Mn K-edge for the same samples are reported in Fig. 4A and B respectively. Peaks beyond the first shell are detectable at both edges.

At the Fe K-edge, the FTs of AFe_450, A_ae and A_450 are very similar to the one of ferrihydrite.[39]

At the Mn K-edge, the FTs of AMn_450, A_ae and A_450 show only one broad and weak peak beyond the first shell indicating a quite disordered structure.

As shown in Fig. 3, the EXAFS oscillations of A_750 and A_900 at both Fe and Mn edges look very similar to those of jacobsite standard.

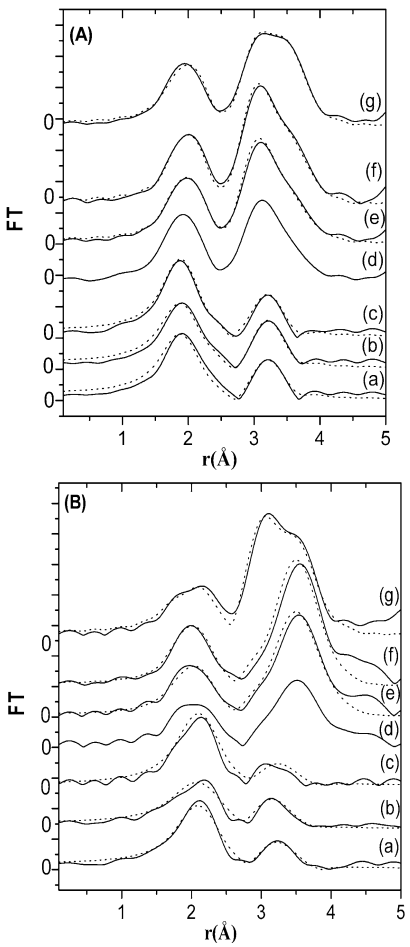

Fig. 4 Fourier transforms of $k^3\chi(k)$ spectra at the Fe K-edge (A) and Mn K-edge (B) from experiment (—) and fit results (···). (A): AFe_450 (a), A_ae (b), A_450 (c), A_750_2h (d), A_750_20h (e), A_900 (f), jacobsite (g). (B): AMn_450 (a), A_ae (b), A_450 (c), A_750_2h (d), A_750_20h (e), A_900 (f), jacobsite (g).

However, the corresponding FT curves of A_750 and A_900 (which are similar to each other) show important differences compared to the pure jacobsite. To understand these differences it is useful to remark that at both edges, the first peak near 2 Å is due to Me–O (Me = Fe, Mn) bond distances, between Me in either tetrahedral or octahedral sites and the oxygens in a close-packed arrangement (see a drawing of the spinel structure in the ESI†). The double peak in the region of 3–4 Å is due to the overlapping of a series of distances, the most important being the distance between Me in two octahedral sites (first maximum) and the distances between Me in two tetrahedral sites and Me in one octahedral and one tetrahedral site (second maximum). In particular, differences are evident in the FT curves of A_750 and A_900 samples in the 3–4 Å region compared to the curve of the pure jacobsite. XRD patterns show that A_750, A_900 and pure jacobsite have the same spinel structure. Therefore, differences in the FTs can be ascribed to a different tetrahedral and/or octahedral site occupation of the cations in the same jacobsite spinel structure.

3.4 EXAFS fitting

The information obtained from the qualitative analysis of EXAFS and XANES oscillations in the aerogels calcined at different temperatures and from the comparison with reference compounds were used as a starting point for a more detailed analysis, performed by fitting of the EXAFS spectra.

3.4.1 Pure jacobsite standard. XANES analysis shows that a fraction of Mn in the pure jacobsite sample is in the oxidation state +3. However, XRD analysis shows that the peaks of this sample correspond to that of $MnFe_2O_4$, which is a partially inverted spinel structure where the iron and manganese cations are distributed between the tetrahedral (A) and octahedral (B) sites available in a close packing of oxygen anions.[40] Therefore, Mn^{3+} is not present as a separate phase but must be included in the sites of the spinel structure. This means that the stoichiometry of the sample cannot be $MnFe_2O_4$ since the higher fraction of 3+ cations must be counterbalanced by a higher amount of O^{2-}. The presence of a non-stoichiometric jacobsite phase is understandable in comparison to γ-Fe_2O_3 (maghemite), which has a spinel structure where all the Fe ions are in the oxidation state 3+. In order to have the same spinel structure as Fe_3O_4 (magnetite), vacancies are present in the spinel structure of maghemite to take into account the lower Fe/O ratio. In particular, the structure of maghemite is a cation-deficient spinel with 21.33 Fe(III) ions distributed among 8 tetrahedral and 16 octahedral sites, and the 2.67 vacancies randomly distributed in the octahedral positions.[41] Since in our jacobsite sample only a fraction of Mn is present as Mn^{3+} the number of vacancies will be lower than in maghemite. Since the number of vacancies is quite low, it will not influence the coordination numbers.

Hence, the pure jacobsite sample has been fitted considering the parameters found in literature for the stoichiometric $MnFe_2O_4$ as starting values. That is, the fitting of the jacobsite sample at both Fe and Mn K-edges was done considering two clusters of atoms, one having the absorbing atom (Fe or Mn) in a tetrahedral site (hereafter called Fe_A and Mn_A) and the

Table 1 Interatomic distances (R), coordination numbers (N) and Debye–Waller factors (σ) obtained by fitting the experimental EXAFS spectra of jacobsite at the Fe and Mn K-edges (R-factors calculated from original data, *R-factors calculated from the backtransforms, as described in the text)

Fe K-edge				Mn K-edge			
Sites B, 65(2)%	R/Å	N	$2\sigma^2$	Sites B, 70(3)%	R/Å	N	$2\sigma^2$
O	2.04(1)	6.0	0.019(1)	O	2.11(1)	6.0	0.030(4)
Fe	3.01(1)	6.0	0.018(1)	Mn	3.00(1)	6.0	0.020(2)
Fe	3.52(1)	6.0	0.022(2)	Mn	3.52(1)	6.0	0.024(2)
O	3.65(6)	2.0	0.021(2)	O	3.65(7)	2.0	0.030(6)
O	3.69(3)	6.0	0.027(1)	O	3.69(3)	6.0	0.030(1)
Sites A, 35(2)%				Sites A, 30(3)%			
O	1.89(1)	4.0	0.018(3)	O	1.92(2)	4.0	0.023(2)
Fe	3.52(1)	12.0	0.022(2)	Mn	3.52(1)	12.0	0.024(3)
O	3.53(3)	12.0	0.030(5)	O	3.53(4)	12.0	0.030(1)
Fe	3.68(4)	4.0	0.030(1)	Mn	3.68(5)	4.0	0.030(1)
	EF = −2.7(1)				EF = −4.5(1)		
	R-factor = 28%				R-factor = 39 %		
	*R-factor = 13%				*R-factor = 25%		

other having the absorbing atom (Fe or Mn) in an octahedral site (hereafter called Fe_B and Mn_B). As Fe and Mn have similar backscattering amplitudes, only Fe backscatterers are considered at the Fe edge and only Mn backscatterers at the Mn edge in order to simplify the fitting. The fitting was performed keeping N_i fixed and allowing small variations of R_i (within the experimental error), whilst $2\sigma_i^2$ and EF were left free to vary. The distribution of Mn^{2+} and Fe^{3+} between tetrahedral (A) sites and octahedral (B) sites was left free to vary subject to the requirements that $x_B = 1 - x_A$ for Mn and $x_B = 2 - x_A$ for Fe, and the totals for Fe and Mn are $x_A = 1$ and $x_B = 2$.

The results of the fitting of the pure jacobsite sample are reported in Fig. 3A/4A and 3B/4B at the Fe and Mn K-edges respectively. The best fitting parameters are reported in Table 1.

At the Fe edge, the first peak near 2 Å is due to two Fe–O bond distances, Fe_A–O (1.89 Å) and Fe_B–O (2.04 Å), corresponding to the tetrahedral sites and the octahedral sites respectively. The double peak in the 3–4 Å region is the overlapping of the contribution from the Fe_B–Fe_B distance (3.01 Å) and a series of other contributions at higher R values (~3.5 Å) from the Fe_A–Fe_A, Fe_A–Fe_B, Fe_B–O and Fe_A–O distances. Similar observations can be made at the Mn edge. The first peak arises from the two distances Mn_A–O (1.92 Å) and Mn_B–O (2.11 Å) due to tetrahedrally and octahedrally coordinated Mn, while the first component of the double peak (3 Å) corresponds to the Mn_B–Mn_B distances and the second component (~3.5 Å) to several contributions, the most important being Mn_A–Mn_A and Mn_A–Mn_B.

The results of the fitting at both the Fe and the Mn edges indicate a degree of inversion i of 0.70.

3.4.2 Aerogels after extraction and aerogels calcined at 450 °C.

The results of the fitting of AFe_450, AMn_450, A_ae and A_450 (at both Fe and Mn edges) are reported in Fig. 3A/4A and 3B/4B respectively. The best-fit parameters are reported in Table 2 (Fe edge) and Table 3 (Mn edge).

At the Fe edge, the EXAFS oscillations of all aerogels are very similar to those of ferrihydrite.[38] Therefore, the same parameters were used for the fitting, *i.e.* one shell of O and three shells of Fe. The R-factor for the fitting of A_450 is lower than those of AFe_450 and A_ae, indicating a less disordered structure.

At the Mn edge, only two shells have been considered: Mn–O at 2.16/2.18 Å ($N \sim 5$) and Mn–Mn at 3.16/3.20 Å ($N \sim 3$). These fitting parameters do not correspond to any of the manganese oxides studied. However, a similar structure around Mn has been observed in mesoporous silicates containing manganese.[42] The Mn environment also has similarities with the structure of $MnSiO_3$ (rhodonite) for which the EXAFS fitting gives a first-shell Mn–O distance of 2.18 Å and coordination number of 5.[43]

3.4.3 Aerogels calcined at 750 and 900 °C.

As shown in Table 4 and Fig. 3 and 4, a good fitting of A_750_20h and A_900 was obtained using the same R and N values used for the pure jacobsite sample. The only parameters left to vary were the Debye–Waller factors and the inversion parameter i. The Debye–Waller factors of the aerogels are higher in general than those of the pure jacobsite standard. The results of the fitting at both the Fe and the Mn edge indicate a degree of inversion of 0.20, significantly different from that of the pure

Table 2 Interatomic distances (R), coordination numbers (N) and Debye–Waller factors (σ) obtained by fitting the experimental EXAFS spectra of AFe_450, A_ae and A_450 at the Fe K-edge

Fe K-edge									
	AFe_450			A_ae			A_450 °C		
	R/Å	N	$2\sigma^2$	R/Å	N	$2\sigma^2$	R/Å	N	$2\sigma^2$
O	1.95(1)	5.1	0.033(2)	1.95(1)	5.1	0.033(1)	1.95(1)	5.1	0.028(1)
Fe	2.87(1)	0.8	0.022(6)	2.87(1)	0.8	0.016(2)	2.87(1)	0.8	0.015(3)
Fe	3.04(1)	2.4	0.024(2)	3.04(1)	2.4	0.019(1)	3.04(1)	2.4	0.020(1)
Fe	3.42(1)	1.5	0.027(7)	3.42(1)	1.5	0.025(5)	3.42(2)	1.5	0.030(1)
	EF = 1.0(4)			EF = 0.2(3)			EF = 0.4(3)		
	R-factor = 32%			R- factor = 31%			R-factor = 23%		

Table 3 Interatomic distances (R), coordination numbers (N) and Debye–Waller factors (σ) obtained by fitting the experimental EXAFS spectra of AMn_450, A_ae and A_450 at the Mn K-edge

Mn K-edge									
	AMn_450			A_ae			A_450 °C		
	R/Å	N	$2\sigma^2$	R/Å	N	$2\sigma^2$	R/Å	N	$2\sigma^2$
O	2.17(1)	5.1	0.038(1)	2.16(1)	5.3	0.050(1)	2.18(1)	5.3	0.035(1)
Mn	3.20(1)	3.0	0.044(2)	3.16(1)	2.8	0.039(2)	3.20(1)	2.8	0.051(4)
	EF = −6.1(2)			EF = −7.6(2)			EF = −5.3(2)		
	R-factor = 23%			R-factor = 27%			R-factor = 29%		

jacobsite standard. Only small differences in Debye–Waller factors were detected between the two samples.

It should be pointed out that the fitting of the A_750_20h and A_900 samples were performed on the assumption that all the EXAFS signal is due to the crystalline phases of the spinel structure. Since the nanoparticles likely grow by metal ions diffusing out of the silica, it is possible that some ions are still inside the silica matrix. However, the number of ions in the silica matrix is certainly quite low, otherwise the EXAFS signals would be significantly modified.

For the samples calcined at 750 °C for 2 h, a good fit was difficult to obtain by using DL_EXCURV. Qualitative analysis of EXAFS and XANES suggested that A_750_2h is in an intermediate stage between A_450 and A_750_20h. Therefore, a different approach was considered: in particular, A_750_2h was simulated by a linear combination of the spectra of A_450 and A_750_20h at both Fe and Mn edge. To this end the program LINCOM,[44] which runs a least-squares routine to minimise the difference between one EXAFS spectrum and the combination of up to nine others, was used in the range 2–12 $Å^{-1}$. The results of the linear combination are shown in Fig. 5. The results of the fitting are quite good at both the Fe and the Mn edges (R-factor = 1%). The results of the fitting at the Fe edge (Fig. 5A) are consistent with the sample comprising around 31% A_450 (ferrihydrite) and 69% A_750_20h (manganese ferrite) while at the Mn edge (Fig. 5B) the fit gives 35% A_450 and 65% A_750_20h (manganese ferrite), associated errors being about 10%.

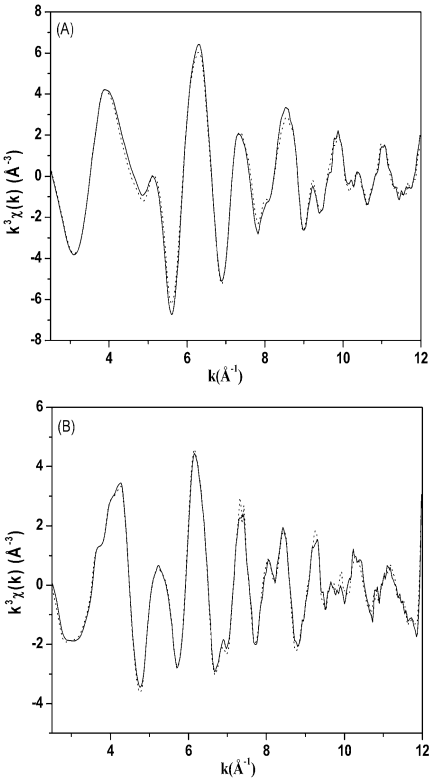

Fig. 5 $k^3\chi(k)$ spectra at (A) the Fe edge, (B) the Mn K-edge for A_750_2h from experiment (—) and linear combination (- - -) of the spectra of A_450 and A_750_20h aerogels.

4. Discussion

EXAFS spectra and fitting parameters of A_ae and A_450 samples at the Fe and Mn edges are similar to the

Table 4 Interatomic distances (R), coordination numbers (N) and Debye–Waller factors (σ) obtained by fitting the experimental EXAFS spectra of A_750 and A_900 at the Fe and Mn K-edge (R-factors calculated from original data, *R-factors calculated from the backtransforms, as described in the text)

Fe K-edge							Mn K-edge						
A_750 20h				A_900			A_750_20h				A_900		
Sites B, 90(3)%	R/Å	N	$2\sigma^2$	R/Å	N	$2\sigma^2$	Sites B, 20(2)%	R/Å	N	$2\sigma^2$	R/Å	N	$2\sigma^2$
O	2.04(1)	6.0	0.026(2)	2.04(1)	6.0	0.025(2)	O	2.11(2)	6.0	0.025(1)	2.11(4)	6.0	0.030(3)
Fe	3.01(1)	6.0	0.020(1)	3.01(1)	6.0	0.018(1)	Mn	3.00(4)	6.0	0.035(1)	3.00(4)	6.0	0.030(4)
Fe	3.52(1)	6.0	0.025(2)	3.52(1)	6.0	0.021(2)	Mn	3.53(2)	6.0	0.029(1)	3.53(3)	6.0	0.025(5)
O	3.65(5)	2.0	0.021(2)	3.65(1)	2.0	0.021(2)	O	3.66(4)	2.0	0.030(1)	3.66(5)	2.0	0.030(3)
O	3.69(2)	6.0	0.030(8)	3.69(1)	6.0	0.030(1)	O	3.69(2)	6.0	0.040(1)	3.69(8)	6.0	0.040(1)
Sites A, 10(3)%							Sites A, 80(2)%						
O	1.89(1)	4.0	0.015(1)	1.89(1)	4.0	0.028(1)	O	2.05(1)	4.0	0.039(2)	2.05(1)	4.0	0.030(3)
Fe	3.52(3)	12.0	0.025(1)	3.52(3)	12.0	0.021(8)	Mn	3.53(2)	12.0	0.029(1)	3.53(4)	12.0	0.025(1)
O	3.53(7)	12.0	0.022(3)	3.53(1)	12.0	0.022(3)	O	3.62(2)	12.0	0.040(6)	3.62(2)	12.0	0.040(2)
Fe	3.68(7)	4.0	0.030(2)	3.68(8)	4.0	0.030(2)	Mn	3.67(2)	4.0	0.030(6)	3.67(2)	4.0	0.030(6)
	EF = −2.6(3)			EF = −2.2(3)				EF = −4.8(4)			EF = −4.3(4)		
	R-factor = 33%			R-factor = 31%				R-factor = 45%			R-factor = 46%		
	*R-factor = 22%			*R-factor = 16%				*R-factor = 26%			*R-factor = 24%		

corresponding aerogels containing only Fe or Mn (AFe_450 and AMn_450) respectively. Therefore, in the aerogels after extraction and up to calcination in argon at 450 °C, two separated phases of iron and manganese are present. The iron phase is certainly ferrihydrite since EXAFS and XANES correspond to this standard. The attribution of the manganese phase is uncertain since EXAFS and XANES profiles do not correspond to any measured standard. Similar results were obtained from a previous study of X-ray absorption on cobalt spinel-ferrite aerogels prepared with an analogous sol–gel procedure. Two separate phases of iron (ferrihydrite) and cobalt in the first stages of heat treatment were identified.[39]

After heat treatment at 750 °C for 2 h, the two separate phases of iron and manganese are partially converted into nanocrystalline manganese ferrite. The conversion is complete as the heating at 750 °C is extended up to 20 h or increased up to 900 °C.

XRD analysis shows that A_750, A_900 and the pure jacobsite sample have the same spinel structure. However, XANES analysis showed that part of Mn in pure jacobsite is present as Mn^{3+}. The amount of Mn^{3+} is probably too low to cause a significant shift of the XRD peak positions. Stoichiometric $MnFe_2O_4$ has a spinel structure belonging to space group *Fd*3*m*. The cubic unit cell is formed by 56 atoms, 32 oxygen anions distributed in a close-packed cubic structure and 24 cations occupying 8 of the 64 tetrahedral sites and 16 of the 32 octahedral sites available.[45] In a *normal* spinel structure, the 8 bivalent cations occupy 8 tetrahedral sites and the 16 trivalent cations occupy 16 octahedral sites whilst in an *inverse* spinel structure the 8 bivalent cations occupy 8 octahedral sites and the 16 trivalent cations are distributed between tetrahedral and octahedral sites.[46] If the bivalent cations are present on both tetrahedral and octahedral sites the spinel is *partially inverted*. The structural formula for a generic spinel compound MFe_2O_4 can be written as:[47]

$$[M_{1-i}Fe_i]^A[M_iFe_{2-i}]^BO_4 \quad (2)$$

where the amounts in brackets represent the average occupancy of A-sites (tetrahedral) and B-sites (octahedral) and i is the inversion parameter. For a *normal* spinel $i = 0$ and for an *inverted* spinel $i = 1$.

Stoichiometric manganese ferrite is reported to be a *partially inverted* spinel structure with manganese atoms predominantly in the tetrahedral sites (low degree of inversion).[48] Typically, $MnFe_2O_4$ prepared using conventional techniques[49] has an inversion degree $i = 0.20$ corresponding to 20% of Fe^{3+} in tetrahedral sites.[27,50] However, different cation distributions over tetrahedral and octahedral sites in manganese ferrites have been associated with different synthetic methods (in particular with different annealing temperatures and cooling rates).[51] Ball-milled $MnFe_2O_4$ was found to have an inversion degree varying from 0.23 to 0.45 depending on the milling time.[52] Artificial manganese ferrites synthesised by pulsed-laser ablation were found to have $i = 0.58$.[53] A value of $i = 0.67$ has been found for $MnFe_2O_4$ prepared by wet-chemical methods[54] and $i = 0.92$ has been found for manganese ferrite synthesised through thermal decomposition of oxalates.[55] The way different synthetic routes affect the cation distribution in the structure is controversial. Some works report a particle-size dependence, showing that the inversion parameter increases with decreasing particle sizes;[56,57] other works report no size dependence showing different degrees of inversion for systems having the same particle size.[58] It has been shown that different preparation conditions of $MnFe_2O_4$ can lead to partial oxidation of manganese ions which can lead to a different distribution of Mn and Fe cations in the crystalline structure.[59] The cation distribution amongst the octahedral and tetrahedral sites affects the physical and chemical properties of the spinel ferrites. In particular, it has been found that the knowledge of the cation site distribution in manganese ferrite is particularly important for magnetic applications.

To the knowledge of the author, an accurate study of the exact degree of inversion of manganese ferrite prepared by sol–gel has not been presented. In this work, a quantitative analysis of the degree of inversion of nanocrystals of a pure jacobsite sample and of nanocomposite $MnFe_2O_4$–SiO_2 aerogels at both Fe and Mn K-edge was performed by fitting the EXAFS oscillations curves. The inversion parameter i has been left free to vary during the fitting, along with the Debye–Waller factors. By fitting i, an accurate determination of the percentage of occupancy of tetrahedral (A) and octahedral (B) sites by Fe^{3+} and Mn^{2+} was achieved.

The fitting of the EXAFS oscillations of the pure jacobsite sample gave an inversion degree of 0.70. The fitting of aerogels A_900 and A_750_20h gave an inversion degree of 0.20. The inversion parameter of the aerogels is the one most commonly found in manganese ferrite synthesised using the conventional solid-state ceramic methods. This is in agreement with our previous work on cobalt-ferrite aerogels,[39] the inversion degrees of which were found to be similar to the most common value.

On the other hand, an inversion parameter of 0.7, a value much higher than the commonly found one, was determined in the pure jacobsite sample which was prepared as a reference following a different technique to the nanocomposite aerogels. Considering that XRD and TEM analysis show that the particles of this sample are larger than those of the nanocomposite, the different inversion degree is hardly related to the particle size as it has been shown that bigger particles give lower degree of inversion.[57] Therefore the different inversion parameter must be due to the partial oxidation of Mn^{2+} to Mn^{3+} which was observed by XANES. As the synthesis of pure jacobsite sample has been done in NaOH solution, it is likely that part of Mn^{2+} has been oxidised to Mn^{3+}, since it has been shown that Mn^{2+} is easily oxidised to Mn^{3+} in highly basic solution.[59] As the Mn^{3+} shows a preference for octahedral sites due to the higher crystal-field stabilisation energy for octahedral coordination,[54] an high inversion degree is expected, as observed in the present case. On the other hand, the calcination of the aerogels was performed in argon avoiding the oxidation of Mn^{2+}, as confirmed by XANES.

It is quite likely that previous reports in which inversion parameters different from the most common value were found in manganese ferrites were due to the presence of some Mn^{3+} which was not apparent. It must be pointed out that standard characterisation techniques, such as XRD, are not able to determine subtle differences like the one observed here. This

proves the advantages of using X-ray absorption techniques in studying the inversion degree in spinels. On the one hand, XANES is capable of determining the oxidation state of the two metals, and on the other hand EXAFS allows one to obtain precise information about the occupancy of the tetrahedral and octahedral sites.

According to eqn (2), the value of $i = 0.70$ which was found in the pure jacobsite sample means that 30% of Mn^{2+} occupies tetrahedral sites and 70% of Mn^{2+} occupies octahedral sites whilst 35% of Fe^{3+} occupies tetrahedral sites and 65% occupies octahedral sites. According to the same equation, in aerogels A_900 and A_750_20h with $i = 0.20$, 80% of Mn^{2+} occupies tetrahedral sites and 20% of Mn^{2+} occupies octahedral sites whilst 10% of Fe^{3+} occupies tetrahedral sites and 90% occupies octahedral sites. It should be noted that this does not take into account the vacancies which should be present in the pure jacobsite sample because of the partial oxidation of Mn^{2+} to Mn^{3+}.

The higher inversion degree of the pure jacobsite sample compared to A_900 and A_750_20h is also in agreement with XANES observations. The higher pre-edge peak of the pure jacobsite sample compared to A_900 and A_750_20h indicates an higher contribution from Fe in tetrahedral sites.

The difference in cation distribution between the pure jacobsite sample and the aerogels is qualitatively evident from the analysis of the FT profiles in the region at about 3 Å, corresponding to the distance between two octahedral metal sites. In Fig. 3A, it is evident that the peak at around 3 Å at the Fe edge is stronger in A_900 and A_750_20h than in the pure jacobsite sample and this is in agreement with the lower inversion degree in the latter. Similarly, at the Mn edge, the peak at 3 Å in the pure jacobsite sample is much more evident than in A_900 and A_750_20h, indicating an higher percentage of manganese in octahedral sites in the former. Therefore, even a qualitative observation of the EXAFS results gives clear information on the inversion degree.

5. Conclusions

In this work we have reported a study of the structural evolution of manganese ferrite aerogels embedded in a silica matrix as a function of temperature. X-Ray absorption spectroscopy was used to analyse the local structures around Fe and Mn atoms. After solvent extraction and calcinations at 450 °C, the aerogels are still highly disordered and contain two separate phases dispersed in the amorphous silica matrix: ferrihydrite and a phase containing manganese. Further heat treatment promotes the formation of the manganese ferrite, which is complete after heating at 750° C for 20 h. The relative distribution of iron and manganese ions between octahedral and tetrahedral sites for the pure manganese ferrite and for A_900 and A_750_20h was determined by fitting of EXAFS data. A clear difference in the cation distribution between a pure jacobsite sample and the aerogels A_750_20h and A_900 was found with inversion-degree values of 0.70 and 0.20 respectively.

The high inversion degree of the pure manganese ferrite sample can be ascribed to the presence of some Mn^{3+}, evidenced by XANES analysis, which prefers the occupation of octahedral sites.

The investigation of $MnFe_2O_4$–SiO_2 nanocomposite aerogels by X-ray absorption spectroscopies provides a means of studying the formation of nanocrystalline ferrites which occurred upon heat treatment under Ar atmosphere. Moreover, insights into the crystal structure of nanosized ferrites such as the inversion degree and the oxidation state could be inferred, which are in turn very useful for interpreting the magnetic behaviour of manganese-ferrite nanocrystals.

Acknowledgements

The authors wish to thank S. G. Fiddy, 7.1 beamline scientist at Daresbury Laboratory, for assistance during data collection and D. Loche for sample preparation. This work was supported by a European Community Sixth Framework Programme Marie Curie Intra-European Fellowship (Contract MEIF-CT-2005-024995).

References

1 E. Tirosh, G. Shemer and G. Markovich, *Chem. Mater.*, 2006, **18**, 465.
2 D. H. Han, H. L. Luo and Z. Yang, *J. Magn. Magn. Mater.*, 1996, **161**, 376.
3 Y. Tae-Jong, K. Jun Sung, K. Byung Geol, Y. Kyeong Nam, C. Myung-Haing and L. Jin-Kyu, *Angew. Chem., Int. Ed.*, 2005, **44**, 1068.
4 C. H. Cunningham, T. Arai, P. C. Yang, M. V. McConnell, J. M. Pauly and S. M. Connolly, *Magn. Reson. Med.*, 2005, **53**, 999.
5 A. K. Giri, K. Pellerin, W. Pongsaksawad, M. Sorescu and S. A. Majetich, *IEEE Trans. Magn.*, 2000, **36**, 3029.
6 A. Goldman, *Modern Ferrite Technology*, Marcel Dekker, New York, 1993.
7 J. Dung, P. G. McCormic and R. Street, *J. Magn. Magn. Mater.*, 1997, **171**, 309.
8 N. S. Gajbhiye and G. Balaji, *Thermochim. Acta*, 2002, **385**, 143.
9 V. M. Burojeanu, L. Fournés, A. Wattiaux, J. Etourneau and E. Segal, *Int. J. Inorg. Mater.*, 2001, **3**, 525.
10 M. A. Denecke, W. Gunber, G. Buxbaum and P. Kuske, *Mater. Res. Bull.*, 1992, **27**, 507.
11 J. B. Silva, C. F. Diniz, R. M. Lago and N. D. S. Mohallem, *J. Non-Cryst. Solids*, 2004, **348**, 201.
12 S. Zhang, D. Dong, Y. Sui, Z. Liu, H. Wang, Z. Qian and W. Su, *J. Alloys Compd.*, 2006, **415**, 257.
13 X.-H. Huang and Z.-H. Chen, *Solid State Commun.*, 1999, **111**, 287.
14 J. W. Long, M. S. Logan, E. E. Carpenter and D. R. Rolison, *J. Non-Cryst. Solids*, 2004, **350**, 182.
15 J. Moscovici, A. Michalowicz, S. Decker, I. Lagadic, K. Latreche and K. Klabunde, *J. Synchrotron Radiat.*, 1999, **6**, 604.
16 J. Moscovici, M. Benzakour, S. Decker, C. Carnes, K. Klabunde and A. Michalowicz, *J. Synchrotron Radiat.*, 2001, **8**, 925.
17 A. V. Chadwick, G. Mountjoy, V. M. Nield, I. J. F. Poplett, M. E. Smith, J. H. Strange and M. G. Tucker, *Chem. Mater.*, 2001, **13**, 1219.
18 A. Corrias, G. Mountjoy, G. Piccaluga and S. Solinas, *J. Phys. Chem. B*, 1999, **103**, 10081.
19 A. Corrias, G. Ennas, G. Mountjoy and G. Paschina, *Phys. Chem. Chem. Phys.*, 2000, **2**, 1045.
20 A. Corrias, M. F. Casula, G. Ennas, S. Marras, G. Navarra and G. Mountjoy, *J. Phys. Chem. B*, 2003, **107**, 3030.
21 A. Corrias, G. Navarra, M. F. Casula, S. Marras and G. Mountjoy, *J. Phys. Chem. B*, 2005, **109**, 13964.
22 *X-Ray Absorption, Principles, Applications, Techniques of EXAFS, SEXAFS and XANES*, ed. D. C. Koningsberger and R. Prins, Wiley, New York, 1987.

23 T. Nakagawa, M. Yuya, T. Tachibana, Y. Takada, H. Nitani, S. Emura and T. A. Yamamoto, *J. Magn. Magn. Mater.*, 2005, **288**, 366.
24 V. G. Harris, N. C. Koon, C. M. Williams, Q. Zhang, M. Abe and J. P. Kirkland, *Appl. Phys. Lett.*, 1996, **68**, 15.
25 C. N. Chinnasamy, A. Yang, S. D. Yoon, K. Hsu, M. D. Schultz, E. E. Carpenter, S. Mukerjee, C. Vittoria and V. G. Harris, *J. Appl. Phys.*, 2007, **101**, 09M509.
26 Z. J. Zhang, Z. L. Wang, C. Chakoumakos and J. S. Yin, *J. Am. Chem. Soc.*, 1998, **120**, 1800.
27 J. Wang, Y. Wu and Y. Zhu, *Int. J. Mod. Phys. B*, 2007, **21**, 723.
28 J.-G. Lee, J. Y. Park and C. S. Kim, *J. Mater. Sci.*, 1998, **33**, 3965.
29 M. F. Casula, D. Loche, S. Marras, G. Paschina and A. Corrias, *Langmuir*, 2007, **23**, 3509.
30 Z. X. Tang, C. M. Sorensen, K. J. Klabunde and G. C. Hadjipanayis, *J. Colloid Interface Sci.*, 1991, **146**(1), 38.
31 A. Bianconi, in *X-Ray Absorption, Principles, Applications, Techniques of EXAFS, SEXAFS and XANES*, ed. D. C. Koningsberger and R. Prins, Wiley, New York, 1987, ch. 11.
32 K. V. Klementiev, *Appl. Phys.*, 2001, **34**, 209.
33 S. Tomic, B. G. Searle, A. Wander, N. M. Harrison, A. J. Dent, J. F. W. Mosselmans and J. E. Inglesfield, *CCLRC Technical Report DL-TR-2005-001*, CCLRC, Warrington, UK, ISSN 1362-0207, 2004.
34 S. J. Gurman, N. Binsted and I. Ross, *J. Phys. C*, 1984, **17**, 143.
35 U. Von Barth and L. Hedin, *J. Phys. C*, 1972, **5**, 1629.
36 E. D. Crozier, *Nucl. Instrum. Methods Phys. Res., Sect. B*, 1997, **133**, 134.
37 Error Report of the International XAFS Society Standards and Criteria Committee, 2000, http://ixs.iit.edu/subcommittee_reports/sc/.
38 PDF card 10-391.
39 D. Carta, G. Mountjoy, G. Navarra, M. F. Casula, D. Loche, S. Marras and A. Corrias, *J. Phys. Chem. C*, 2007, **111**, 6308.
40 T. J. Inoue, *Electrochem. Soc. Jpn.*, 1955, **23**, 24.
41 A. N. Shmakov, G. N. Kryukova, S. V. Tsybulya, A. L. Chuvilin and L. P. Solovyeva, *J. Appl. Crystallogr.*, 1995, **28**, 141.
42 N. N. Tušar, N. Z. Logar, G. Vlaic, I. Arčon, D. Arčon, N. Daneu and V. Kaučič, *Microporous Mesoporous Mater.*, 2005, **82**, 129.
43 D. A. McKeown, W. K. Kot, H. Gan and I. L. Pegg, *J. Non-Cryst. Solids*, 2003, **328**, 71.
44 *LINCOM, Linear combination program from CCP3, Collaborative Computational Project 3*, Daresbury Laboratory, Warrington, UK.
45 K. E. Sickafus and J. M. Wills, *J. Am. Ceram. Soc.*, 1999, **82**(12), 3279.
46 V. G. Harris, N. C. Koon, C. M. Williams, Q. Zhang, M. Abe and J. P. Kirkland, *Appl. Phys. Lett.*, 1996, **68**, 15.
47 Z. J. Zhang, Z. L. Wang, B. C. Chakoumakos and J. S. Yin, *J. Am. Chem. Soc.*, 1998, **120**, 1800.
48 X. Zuo, A. Yang, S. Yoon, J. A. Christodoulides, V. G. Harris and C. Vittoria, *J. Appl. Phys.*, 2005, **97**, 10G103.
49 F. W. Harrison, W. P. Osmond and R. W. Teale, *Phys. Rev.*, 1957, **105**, 5.
50 E. Kravtsov, D. Haskel, A. Cady, A. Yang, C. Vittoria, X. Zuo and V. G. Harris, *Phys. Rev. B*, 2006, **74**, 104114.
51 T. A. S. Ferreira, J. C. Waerenborgh, M. H. R. M. Mendonça, M. R. Nunes and F. M. Costa, *Solid State Sci.*, 2003, **5**, 383.
52 M. H. Mahmoud, H. H. Hamdeh, J. C. Ho, M. J. O'Shea and J. C. Walker, *J. Magn. Magn. Mater.*, 2000, **220**, 139.
53 A. Yang, V. G. Harris, S. Calvin, X. Zuo and C. Vittoria, *IEEE Trans. Magn.*, 2004, **40**, 4.
54 J. P. Chen, C. M. Sorensen, K. J. Klabunde, G. C. Hadjipanayis, E. Devlin and A. Kostikas, *Phys. Rev. B*, 1996, **54**, 13.
55 M. A. Gabal and S. S. Ata-Allah, *J. Phys. Chem. Solids*, 2004, **65**, 995.
56 P. J. Van der Zaag, V. A. M. Brabers, M. T. Johnson, A. Noordermeer and P. F. Bongers, *Phys. Rev. B*, 1995, **51**, 17.
57 M. H. Mahmoud, H. H. Hamdeh, A. I. Abdel-Mageed, A. M. Abdallah and M. K. Fayek, *Phys. B*, 2000, **291**, 49.
58 G. U. Kulkarni, K. R. Kanna, T. Arunarkavalli and C. N. R. Rao, *Phys. Rev. B*, 1994, **49**, 724.
59 Z. J. Zhang, Z. L. Wang, B. C. Chakoumakos and J. S. Yin, *J. Am. Chem. Soc.*, 1998, **120**, 1800.